IEEE TRANSACTIONS ON MICROWAVE THEORY AND TECHNIQUES, VOL. 39, NO. 3, MARCH 1991

# Elimination of Vector Parasites in Finite Element Maxwell Solutions

Keith D. Paulsen, *Member, IEEE*, and Daniel R. Lynch

*Abstract*—**The vector parasite problem is studied in the context of finite element solutions of Maxwell's equations for driven boundary-value problems. An expanded weak form is introduced which combines the divergence equation with the conventional weak form of the double-curl equation. This new form is related to penalty methods where the penalty or weighting factor varies with the dielectric constant. The resulting algebraic system is identical to the Galerkin–Helmholtz operator on homogeneous subregions. Normal and tangential boundary conditions arise in terms of the divergence and curl of the field on the boundary.**

**Computational results show the occurrence of two distinct types of parasitic modes in driven problems and their elimination with the new formulation. Practical observations concerning the conditions which provoke spurious modes in these problems are reported.**

**Spurious solutions also arise from improper or unphysical boundary conditions, and the importance of careful specification of boundary-value problems is illustrated. Most conceptual difficulties with boundary conditions *per se* are removed when hybrid methods are used to couple the interior finite element solution to the exterior problem, which focuses attention on the physics of the source distribution.**

## I. INTRODUCTION

THE occurrence of spurious computational modes in finite element (FEM) vector wave equation solutions has been known for some time [1], [2] and suppression of such erroneous calculations is still a subject of great interest [3], [4]. The majority of research to date on parasitic modes has been in the context of eigenvalue problems; hence, the notion of computing nonphysical solutions has been closely tied to modal analysis. The most consistently noted feature of these fictitious solutions has been their divergent nature in cases where the physical solution is completely solenoidal. Additional vector parasites have been reported with wavelengths at or near the mesh scale [5].

Reports of spurious solutions in vector boundary-value problems, on the other hand, have been sparse; thus FEM formulations for driven problems have largely been perceived to be free of these computational difficulties. In fact, this presumed immunity of driven problems has been suggested as a possible remedy to the eigenvalue dilemma [6], [7]. Recently, however, Crowley *et al.* [8], Pinchuk *et al.* [9], and Wong and Cendes [10], [11] have shown that careful selection of the forcing term can lead to completely erroneous double-curl FEM computations for some simple boundary value problems. Although our earlier double-curl FEM computations [12], [13] did not reveal any degradations that could be attributable to nonphysical solutions, the insightful comments by Crowley and Silvester [14] plus the general lack of studies on spurious vector components of FEM solutions to boundary-value problems have motivated us to investigate this issue more closely.

The traditional approaches to removing spurious vector modes have been classified as (1) those which modify the FEM basis and (2) those which modify the FEM functional or weak form. Examples of modifications of the basis can be found in [8], [15], and [16]. Several strategies exist including forcing the basis to have exactly zero divergence. To achieve zero divergence, special care is required to guarantee the continuity of $\hat{n}\cdot\epsilon^* E$ at interelement *boundaries* as well as on element interiors. Otherwise the divergence of the basis vanishes at best in the weak sense as is the case for "edge elements" [17]. We have investigated the importance of normal field continuity in inhomogeneous calculations [18] and have concluded that strong enforcement (as can be achieved with the bases used here) produces solutions with improved accuracy, especially near dielectric interfaces, relative to those produced with edge elements.

Modification of the FEM functional in order to remove spurious solutions has been associated with the so-called penalty method [19], [20]. In the present context, this amounts to adding a weighted divergence equation $\nabla\cdot\epsilon^* E = 0$ to the double-curl equation. In weighted residual or variational formulations the cost of divergence is then "penalized" by using a large weight. In terms of the spectrum of the discretized matrix equation, the penalty factor is perceived to shift the eigenvalues out of the range of interest [21], [22], thus eliminating the effects of divergent modes. The key to success with the penalty method has been in the choice of the correct penalty factor—values too small or too large cause (or do not eliminate) unacceptable results. Unfortunately, the choice of a suitable penalty factor has tended to be problem-specific and no systematic approach or rationale for selecting this parameter for general problems has been put forth to date.

The strategy that we propose for eliminating spurious computational modes in vector FEM boundary-value problems is to modify the weak form of the governing vector equation in a manner closely related to the penalty term alteration discussed above. However, rather than leaving the penalty factor arbitrary and problem-dependent, we prescribe a weak form which in effect reduces the algebraic double-curl operator to a Laplacian on homogeneous subre-

---

Manuscript received January 12, 1990; revised October 16, 1990. This work was supported by the U.S. National Science Foundation under Grant CEE-8352226 and by the National Institutes of Health under Grants NIH/NCI CA 45357 and CA37245.

The authors are with the Thayer School of Engineering, Dartmouth College, Hanover, NH 03755.

IEEE Log Number 9042345.

0018-9480/91/0300-0395$01.00

gions. We have demonstrated the importance of the resulting Helmholtz structure by analyzing 2-D dispersion relations arising from both finite-difference and finite element discretizations of the Maxwell equations on homogeneous, regular meshes. As we show in [23] the Helmholtz algebra has monotonic dispersion curves which mimic their analytic counterparts such that proper specification of physical boundary conditions ensures suppression of spurious "divergence" modes whereas the double-curl and penalty algebras have double-valued dispersion surfaces such that the synthesis of physical and spurious modes is unavoidable in problems driven by physically correct boundary conditions.

Herein, we qualitatively confirm these idealized dispersion analyses in the practical context of computing FEM solutions to inhomogeneous boundary-value problems on irregular geometries. Specifically, we demonstrate the presence of the two predicted vector parasites [23] in our original formulation [12] and their removal with the proposed weak-form modification. In addition we illustrate the introduction of spurious solutions through improperly posed boundary conditions, which in subtle ways can dictate unphysical behavior by themselves.

## II. The Expanded Weak Form

Our original formulation for vector boundary-value FEM solutions [12] proceeds directly from the double-curl equation

$$\nabla\times\left(\frac{1}{i\omega\mu}\nabla\times \boldsymbol{E}\right)+i\omega\epsilon^{*}\boldsymbol{E}=0 \tag{1}$$

for the electric field, where $\epsilon^{*}=\epsilon+i\sigma/\omega$ is the complex permittivity. The weak form of (1) which we have used is

$$\left\langle\left(\frac{1}{i\omega\mu}\nabla\times \boldsymbol{E}\right)\times\nabla\phi_i\right\rangle+\langle i\omega\epsilon^{*}\boldsymbol{E}\phi_i\rangle = -\oint\frac{1}{i\omega\mu}\hat{\boldsymbol{n}}\times(\nabla\times \boldsymbol{E})\phi_i\,ds \tag{2}$$

where $\langle\ \rangle$ and $\oint$ indicate integration over the problem domain and boundary, respectively, and $\phi_i$ are the conventional linear or bilinear basis functions associated with scalar FEM formulations. At interior element boundaries where no physical sources exist, $(1/i\omega\mu)\hat{\boldsymbol{n}}\times(\nabla\times \boldsymbol{E})$, or equivalently $\hat{\boldsymbol{n}}\times \boldsymbol{H}$, is continuous and therefore the boundary integral vanishes; while at sources on the interior, the discontinuity in $\hat{\boldsymbol{n}}\times \boldsymbol{H}$ is replaced by physical current $\boldsymbol{J}$. At outer boundary nodes, either the exterior solution must be coupled to $\hat{\boldsymbol{n}}\times \boldsymbol{H}$ or else the problem terminated as a boundary value problem by specification of $\hat{\boldsymbol{n}}\times \boldsymbol{E}$, $\hat{\boldsymbol{n}}\times \boldsymbol{H}$, or an equivalent current.

Expansion of (2) in the basis $\phi_i$ leads to the Galerkin weak form $\boldsymbol{A}_{ij}\boldsymbol{E}_j=\boldsymbol{R}_i$, in which $\boldsymbol{A}$ comprises complex $3\times3$ submatrices

$$\boldsymbol{A}_{ij}=\begin{pmatrix}
\left\langle\frac{1}{i\omega\mu}\left(\frac{\partial\phi_j}{\partial y}\frac{\partial\phi_i}{\partial y}+\frac{\partial\phi_j}{\partial z}\frac{\partial\phi_i}{\partial z}\right)\right\rangle+\langle i\omega\epsilon^{*}\phi_i\phi_j\rangle & \left\langle-\frac{1}{i\omega\mu}\frac{\partial\phi_j}{\partial x}\frac{\partial\phi_i}{\partial y}\right\rangle & \left\langle-\frac{1}{i\omega\mu}\frac{\partial\phi_j}{\partial x}\frac{\partial\phi_i}{\partial z}\right\rangle\\
\left\langle-\frac{1}{i\omega\mu}\frac{\partial\phi_j}{\partial y}\frac{\partial\phi_i}{\partial x}\right\rangle & \left\langle\frac{1}{i\omega\mu}\left(\frac{\partial\phi_j}{\partial x}\frac{\partial\phi_i}{\partial x}+\frac{\partial\phi_j}{\partial z}\frac{\partial\phi_i}{\partial z}\right)\right\rangle+\langle i\omega\epsilon^{*}\phi_i\phi_j\rangle & \left\langle-\frac{1}{i\omega\mu}\frac{\partial\phi_j}{\partial y}\frac{\partial\phi_i}{\partial z}\right\rangle\\
\left\langle-\frac{1}{i\omega\mu}\frac{\partial\phi_j}{\partial z}\frac{\partial\phi_i}{\partial x}\right\rangle & \left\langle-\frac{1}{i\omega\mu}\frac{\partial\phi_j}{\partial z}\frac{\partial\phi_i}{\partial y}\right\rangle & \left\langle\frac{1}{i\omega\mu}\left(\frac{\partial\phi_j}{\partial x}\frac{\partial\phi_i}{\partial x}+\frac{\partial\phi_j}{\partial y}\frac{\partial\phi_i}{\partial y}\right)\right\rangle+\langle i\omega\epsilon^{*}\phi_i\phi_j\rangle
\end{pmatrix}. \tag{3}$$

Note that the double-curl identity $\nabla\times\nabla\times \boldsymbol{E}=-\nabla^2\boldsymbol{E}+\nabla(\nabla\cdot \boldsymbol{E})$ is commonly invoked along with the condition $\nabla\cdot \boldsymbol{E}=0$ to convert (1) to the Helmholtz equation on homogeneous regions; however, the derived algebraic form (3) lacks the crucial divergence information and therefore does not display the conventional Galerkin–Helmholtz structure.

The modified weak form introduced here is based on the expanded PDE

$$\nabla\times\left(\frac{1}{i\omega\mu}\nabla\times \boldsymbol{E}\right)-\nabla\left(\frac{1}{i\omega\mu\epsilon^{*}}\nabla\cdot\epsilon^{*}\boldsymbol{E}\right)+i\omega\epsilon^{*}\boldsymbol{E}=0. \tag{4a}$$

The spatial discretization is handled by using the method of weighted residuals:

$$\left\langle\phi_i\nabla\times\left(\frac{1}{i\omega\mu}\nabla\times \boldsymbol{E}\right)\right\rangle-\left\langle\phi_i\nabla\left(\frac{1}{i\omega\mu\epsilon^{*}}\nabla\cdot\epsilon^{*}\boldsymbol{E}\right)\right\rangle+\langle i\omega\epsilon^{*}\boldsymbol{E}\phi_i\rangle=0 \tag{4b}$$

where $\langle\ \rangle$, $\oint$, and $\phi_i$ are defined as in (2). Use of the identities

$$\left\langle\phi_i\nabla\times\left(\frac{1}{i\omega\mu}\nabla\times \boldsymbol{E}\right)\right\rangle=\oint\hat{\boldsymbol{n}}\times\left(\frac{1}{i\omega\mu}\nabla\times \boldsymbol{E}\right)\phi_i\,ds-\left\langle\nabla\phi_i\times\left(\frac{1}{i\omega\mu}\nabla\times \boldsymbol{E}\right)\right\rangle \tag{4c}$$

$$\left\langle\phi_i\nabla\left(\frac{1}{i\omega\mu\epsilon^{*}}\nabla\cdot\epsilon^{*}\boldsymbol{E}\right)\right\rangle=\oint\hat{\boldsymbol{n}}\frac{1}{i\omega\mu\epsilon^{*}}(\nabla\cdot\epsilon^{*}\boldsymbol{E})\phi_i\,ds-\left\langle\frac{1}{i\omega\mu\epsilon^{*}}(\nabla\cdot\epsilon^{*}\boldsymbol{E})\nabla\phi_i\right\rangle \tag{4d}$$

leads to the associated weak form:

$$\left\langle\frac{1}{i\omega\mu}(\nabla\times \boldsymbol{E})\times\nabla\phi_i\right\rangle+\left\langle\frac{1}{i\omega\mu\epsilon^{*}}(\nabla\cdot\epsilon^{*}\boldsymbol{E})\nabla\phi_i\right\rangle+\langle i\omega\epsilon^{*}\boldsymbol{E}\phi_i\rangle = -\oint\frac{1}{i\omega\mu}\hat{\boldsymbol{n}}\times(\nabla\times \boldsymbol{E})\phi_i\,ds+\oint\hat{\boldsymbol{n}}\frac{\nabla\cdot\epsilon^{*}\boldsymbol{E}}{i\omega\mu\epsilon^{*}}\phi_i\,ds \tag{5}$$

assuming continuity of $\nabla\cdot\epsilon^*\boldsymbol{E}$ at interior element boundaries. Note that the weak form (2) displays only $\nabla\times\boldsymbol{E}$ as the natural boundary condition; ideally the double-curl equation guarantees the condition $\nabla\cdot\boldsymbol{E}=0$, although as demonstrated here and in [23] this is not realized numerically due to parasites. The expanded weak form (5) displays both $\nabla\times\boldsymbol{E}$ and $\nabla\cdot\epsilon^*\boldsymbol{E}$ as natural boundary conditions. As will be shown in the following sections, the process of specifying boundary conditions for (5) involves only physical reasoning whereas the use of (2) relies on the removal of unpredictable spurious behavior which depends fundamentally on the mesh spacing.

Adopting a Galerkin-style expansion for $\boldsymbol{E}$ in terms of the scalar basis $\phi_j$ as above produces the same algebraic form $\boldsymbol{A}_{ij}\boldsymbol{E}_j=\boldsymbol{R}_i$ with $\boldsymbol{A}_{ij}$ modified as

$$\boldsymbol{A}_{ij}=\begin{bmatrix} \left\langle \frac{1}{i\omega\mu}\left(\frac{\partial\phi_j}{\partial y}\frac{\partial\phi_i}{\partial y}+\frac{\partial\phi_j}{\partial z}\frac{\partial\phi_i}{\partial z}+\frac{\partial\phi_j}{\partial x}\frac{\partial\phi_i}{\partial x}\right)\right\rangle+\left\langle i\omega\epsilon^*\phi_i\phi_j\right\rangle & \left\langle \frac{1}{i\omega\mu}\left(-\frac{\partial\phi_j}{\partial x}\frac{\partial\phi_i}{\partial y}+\frac{\partial\phi_j}{\partial y}\frac{\partial\phi_i}{\partial x}\right)\right\rangle & \left\langle \frac{1}{i\omega\mu}\left(-\frac{\partial\phi_j}{\partial x}\frac{\partial\phi_i}{\partial z}+\frac{\partial\phi_j}{\partial z}\frac{\partial\phi_i}{\partial x}\right)\right\rangle \\ \left\langle \frac{1}{i\omega\mu}\left(-\frac{\partial\phi_j}{\partial y}\frac{\partial\phi_i}{\partial x}+\frac{\partial\phi_j}{\partial x}\frac{\partial\phi_i}{\partial y}\right)\right\rangle & \left\langle \frac{1}{i\omega\mu}\left(\frac{\partial\phi_j}{\partial x}\frac{\partial\phi_i}{\partial x}+\frac{\partial\phi_j}{\partial z}\frac{\partial\phi_i}{\partial z}+\frac{\partial\phi_j}{\partial y}\frac{\partial\phi_i}{\partial y}\right)\right\rangle+\left\langle i\omega\epsilon^*\phi_i\phi_j\right\rangle & \left\langle \frac{1}{i\omega\mu}\left(-\frac{\partial\phi_j}{\partial y}\frac{\partial\phi_i}{\partial z}+\frac{\partial\phi_j}{\partial z}\frac{\partial\phi_i}{\partial y}\right)\right\rangle \\ \left\langle \frac{1}{i\omega\mu}\left(-\frac{\partial\phi_j}{\partial z}\frac{\partial\phi_i}{\partial x}+\frac{\partial\phi_j}{\partial x}\frac{\partial\phi_i}{\partial z}\right)\right\rangle & \left\langle \frac{1}{i\omega\mu}\left(-\frac{\partial\phi_j}{\partial z}\frac{\partial\phi_i}{\partial y}+\frac{\partial\phi_j}{\partial y}\frac{\partial\phi_i}{\partial z}\right)\right\rangle & \left\langle \frac{1}{i\omega\mu}\left(\frac{\partial\phi_j}{\partial x}\frac{\partial\phi_i}{\partial x}+\frac{\partial\phi_j}{\partial y}\frac{\partial\phi_i}{\partial y}+\frac{\partial\phi_j}{\partial z}\frac{\partial\phi_i}{\partial z}\right)\right\rangle+\left\langle i\omega\epsilon^*\phi_i\phi_j\right\rangle \end{bmatrix}. \tag{6}$$

Alone, the diagonal terms of (6) may be recognized as a conventional Galerkin rendering of the Helmholtz equation for the three scalar components of $\boldsymbol{E}$, separately. Further, the off-diagonal terms *vanish* on the interior of homogeneous subregions, leaving *only* the Helmholtz operator which has the spurious-mode-resistant properties detailed in [23]. This can be seen as follows. First, note that the off-diagonals are the components of $\langle\nabla\phi_i\times\nabla\phi_j\rangle$. The contribution to this integral over a single element, $\langle\ \rangle^e$, may be integrated by parts as follows:

$$\langle\nabla\phi_i\times\nabla\phi_j\rangle^e=\left\langle\nabla\times(\phi_i\nabla\phi_j)\right\rangle^e-\left\langle(\nabla\times\nabla\phi_j)\phi_i\right\rangle^e. \tag{7}$$

The integrand of the last term vanishes identically at all points on the interior of conventional elements. The surviving right-side term may be converted to a boundary integral by the curl theorem, the result of which is

$$\langle\nabla\phi_i\times\nabla\phi_j\rangle^e=\oint^e\hat{\boldsymbol{n}}\times(\phi_i\nabla\phi_j)\,ds. \tag{8}$$

For conventional $C^0$ elements, both $\phi_i$ and its tangential derivatives are continuous at interior element boundaries; therefore on assembly (summation over all elements) only the integrals on exterior boundary segments survive cancellation:

$$\langle\nabla\phi_i\times\nabla\phi_j\rangle=\oint\hat{\boldsymbol{n}}\times(\phi_i\nabla\phi_j)\,ds. \tag{9}$$

Inspection of (9) reveals that the boundary integral vanishes if either node $i$ or $j$ is an interior node (since either $\phi_i$ or $\hat{\boldsymbol{n}}\times\nabla\phi_j$ will be zero on the exterior boundary). It follows that the off-diagonal terms in $\boldsymbol{A}_{ij}$ vanish unless both $i$ and $j$ are boundary nodes. In effect, the expanded weak form (5) produces a Galerkin–Helmholtz algebraic form on the interior:

$$\boldsymbol{A}_{ij}=\left\langle\frac{1}{i\omega\mu}\nabla\phi_j\cdot\nabla\phi_i+i\omega\epsilon^*\phi_i\phi_j\right\rangle\boldsymbol{I} \tag{10}$$

with modifications at the boundaries as expressed in (5) which allow the curl and divergence of the field to appear as natural boundary conditions.

When numerical quadrature is used, the curl theorem does not apply exactly; nevertheless we obtain the analogous result

$$\left[\nabla\phi_i\times\nabla\phi_j\right]=\oint\hat{\boldsymbol{n}}\times(\phi_i\nabla\phi_j)\,ds+\mathscr{E}_{ij} \tag{11}$$

where $[\ ]$ is the quadrature approximation to $\langle\ \rangle$, and $\mathscr{E}_{ij}$ is the quadrature error:

$$\mathscr{E}_{ij}\equiv\left[\nabla\times(\phi_i\nabla\phi_j)\right]-\left\langle\nabla\times(\phi_i\nabla\phi_j)\right\rangle. \tag{12}$$

Irrespective of quadrature, all row and column sums of the off-diagonal terms in $\boldsymbol{A}_{ij}$ vanish, a consequence of the property $\Sigma\phi_i=1$ which holds at all points in simple elements.

Finally, we obtain the discrete energy balance as in [12] by multiplying (5) by $\bar{\boldsymbol{E}}_i$ (complex conjugate of $\boldsymbol{E}_i$) and summing. The result is

$$\left\langle\frac{(\nabla\cdot\epsilon^*\boldsymbol{E})(\nabla\cdot\bar{\boldsymbol{E}})}{2i\omega\mu\epsilon^*}+\frac{(\nabla\times\boldsymbol{E})\cdot(\nabla\times\bar{\boldsymbol{E}})}{2i\omega\mu}+i\omega\epsilon^*\frac{\boldsymbol{E}\cdot\bar{\boldsymbol{E}}}{2}\right\rangle=\oint\left(\frac{\bar{\boldsymbol{E}}\times\boldsymbol{H}}{2}\right)\cdot\hat{\boldsymbol{n}}\,ds+\oint\frac{(\nabla\cdot\epsilon^*\boldsymbol{E})\bar{\boldsymbol{E}}\cdot\hat{\boldsymbol{n}}}{2i\omega\mu\epsilon^*}\,ds. \tag{13}$$

The real part of (13) corresponding to the time-averaged component of the power balance is

$$\left\langle\sigma\frac{\boldsymbol{E}\cdot\bar{\boldsymbol{E}}}{2}\right\rangle+\mathrm{Re}\left(\oint\left(\frac{\boldsymbol{E}\times\bar{\boldsymbol{H}}}{2}\right)\cdot\hat{\boldsymbol{n}}\,ds+\oint\frac{(\nabla\cdot\epsilon^*\boldsymbol{E})\bar{\boldsymbol{E}}\cdot\hat{\boldsymbol{n}}}{2i\omega\mu\epsilon^*}\,ds\right)=0. \tag{14}$$

This is unchanged from its original form when either $\nabla\cdot\epsilon^*\boldsymbol{E}$ or $\boldsymbol{E}\cdot\hat{\boldsymbol{n}}$ vanishes on the boundary. Additional terms appear

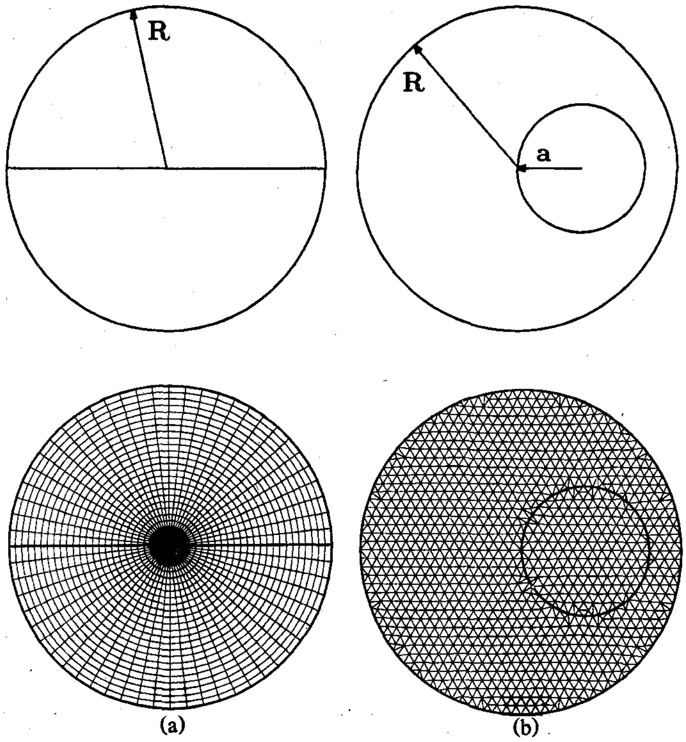

(a) (b)

Fig. 1. (a) A cylinder ($R = 25$ cm) split into two regions having different complex wavenumbers. The computational FEM mesh is shown. (b) A smaller off-center cylinder ($a = 10$ cm) embedded in a larger cylinder ($R = 25$ cm). Different complex wavenumbers are used to characterize the two regions. The computational FEM mesh is shown.

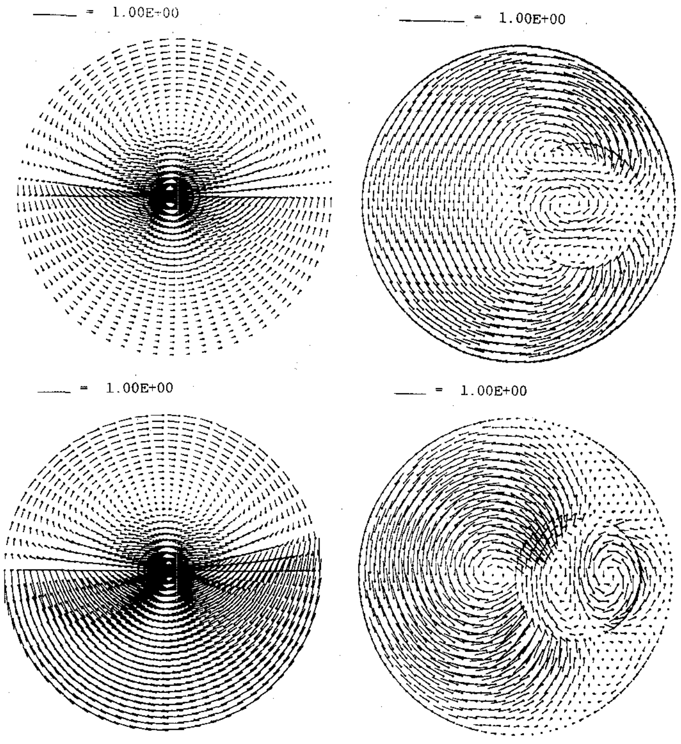

(a) (b)

Fig. 2. (a) Benchmark solution for the split cylinder case (Fig. 1(a)) where $k^2_{\text{Top}} = (2.08, 20.53)$ and $k^2_{\text{Bottom}} = (0.074, 0.0)$. Vector plots of $\mathrm{Re}(\boldsymbol{E})$ (top) and $\mathrm{Im}(\boldsymbol{E})$ (bottom) are shown. Vector length is proportional to strength (max scaled to unity). (b) Benchmark solution for the off-center cylinder case (Fig. 1(b)) where $k^2_{\text{Inner}} = (2000, 0.0)$ and $k^2_{\text{Outer}} = (196.1, 39.22)$. Vector plots of $\mathrm{Re}(\boldsymbol{E})$ (top) and $\mathrm{Im}(\boldsymbol{E})$ (bottom) are shown. Vector length is proportional to strength (max scaled to unity).

in the imaginary part of (13) (the reactive power balance) as follows:

$$\left\langle \frac{(\nabla\cdot\epsilon^*\boldsymbol{E})(\nabla\cdot\bar{\boldsymbol{E}})}{2\omega\mu\epsilon^*} + \frac{(\nabla\times\boldsymbol{E})\cdot(\nabla\times\bar{\boldsymbol{E}})}{2\omega\mu} - \omega\epsilon\frac{\boldsymbol{E}\cdot\bar{\boldsymbol{E}}}{2}\right\rangle - \mathrm{Im}\left(\oint\left(\frac{\boldsymbol{E}\times\bar{\boldsymbol{H}}}{2}\right)\cdot\hat{\boldsymbol{n}}\,ds - \oint\frac{(\nabla\cdot\epsilon^*\boldsymbol{E})\bar{\boldsymbol{E}}\cdot\hat{\boldsymbol{n}}}{2i\omega\mu\epsilon^*}\,ds\right) = 0. \quad (15)$$

## III. RESULTS

This section contains results for 2-D boundary-value and hybrid problems where spurious solutions appear when (2) is used, but are removed in the case where (5) governs. Code validations of our earlier formulation involved a test problem consisting of concentric cylinders of dissimilar media excited with a uniform $\boldsymbol{H}$ imposed at the outer boundary. While we have yet to find any parasitic solutions with our original formulation in this case, it is a simple boundary-value problem which involves only one radial mode and, in the terminology of Crowley and Silvester [14], such an excitation is probably orthogonal to potentially spurious modes; hence they may not appear as our numerical experiments, to date, have confirmed.

Two variants on this geometry, shown in Fig. 1, are now studied. As before, a uniform $\boldsymbol{H}$ is imposed at the outer cylinder boundary, but these geometries, in general, excite all radial and circumferential modes; hence they are better benchmark problems for studying corrupted solutions. Further, by examining a wide range of electrical properties in the two regions, the effects of exciting various weighted combinations of the modes can be investigated. Because the geometries are not amenable to analytical boundary-value solution, a reference standard is derived by first numerically solving for $\boldsymbol{H}$, followed by subsequent Galerkin treatment of $\nabla\times\boldsymbol{H} = -i\omega\epsilon^*\boldsymbol{E}$ to produce $\boldsymbol{E}$ [24]. Since $\boldsymbol{H}$ is computed with a scalar Helmholtz equation, it can be presumed free of spurious modes of the type investigated herein. Further, $\boldsymbol{E}$ is obtained by curling the $\boldsymbol{H}$ solution, which also guarantees that no irrotational components will exist; hence, computation of $\boldsymbol{E}$ in this fashion can be regarded as only limited in its accuracy by the resolution of the mesh.

Parts (a) and (b) of Fig. 2 show sample solutions of $\boldsymbol{E}$ computed in this "benchmark" manner on the geometries in Fig. 1(a) and (b), respectively. When (2) is used, however, the FEM solution can be severely corrupted. The spurious solutions shown in Fig. 3 are representative of some of the more shocking results that we have obtained solving (2) on the geometries in Fig. 1. The solutions in Fig. 3 illustrate the occurrence of two apparently different types of parasites. The first, shown in Fig. 3(a), is well resolved and exhibits distinct divergence. The second, shown in Fig. 3(b), appears as node-to-node oscillations at the mesh scale, suggesting the presence of unresolved waves at or near the mesh cutoff point (i.e., $\lambda = 2\Delta x$). These two classes of parasitic solutions are consistent with those reported by others in the eigenvalue problem context [5] and in a companion paper [23] have been referred to as type A (i.e., Fig. 3(a)) and type B (i.e., Fig. 3(b)), respectively.

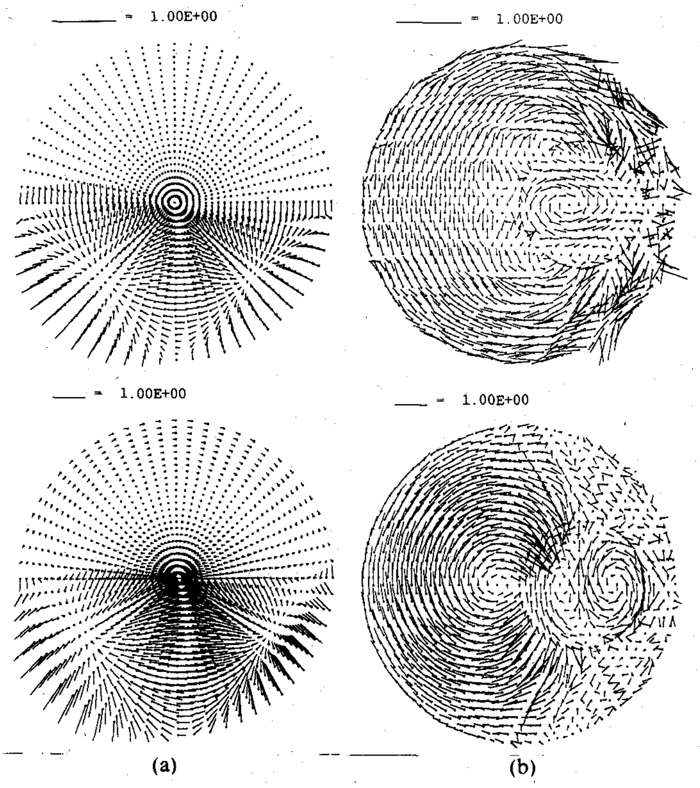

Fig. 3. (a) Same as Fig. 2(a) except that FEM solution using the conventional double-curl formulation (eq. (2)) governs. The observed parasite is well resolved and shows clear divergent behavior. (b) Same as Fig. 2(b) except that FEM solution using the conventional double-curl formulation (eq. (2)) governs. The observed parasite is poorly resolved, showing node-to-node oscillations.

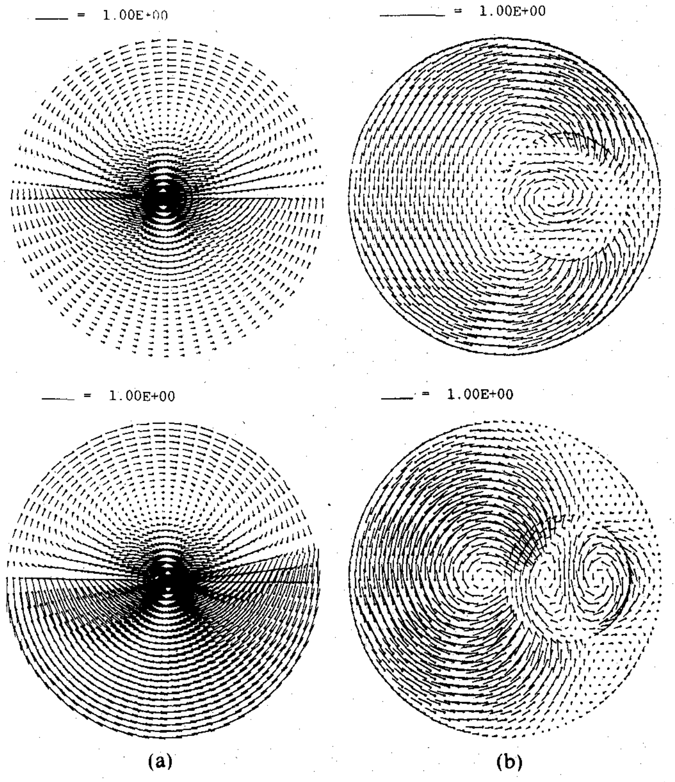

Fig. 4. (a) Same as Fig. 2(a) except that FEM solution using the extended weak form (eq. (5)) governs. The well-resolved divergent parasite of Fig. 3(a) is removed. $\boldsymbol{E}\cdot\hat{\boldsymbol{n}} = 0$ is explicitly enforced at the outer boundary. The solution is essentially identical to the benchmark solution of Fig. 2(a). (b) Same as Fig. 2(b) except that FEM solution using the extended weak form (eq. (5)) governs. The node-to-node oscillatory parasite of Fig. 3(b) is removed. The homogeneous natural boundary condition $\nabla\cdot\epsilon^*\boldsymbol{E} = 0$ is applied at the outer boundary. The solution is essentially identical to the benchmark solution of Fig. 2(b).

The factors which appear to determine the severity of the corruptions in FEM solutions via (2) are the magnitude and phase of the complex-valued wavenumbers of the respective media and the size of their ratio. An extensive search of the parameter space has been conducted where the ranges over which these factors have been varied are $|k^2|\Delta x^2 \approx 10^{-5} \to 0.5$, $\sigma/\omega\epsilon = 0 \to 20$, and $|k^2|_{\text{outer}}/|k^2|_{\text{inner}} = 0.1 \to 10$. Generally, the most prognostic indicator has been the magnitude; however, the size ratio is also important. If $|k^2|\Delta x^2 > 0.02$ and the size ratio is near unity ($|k^2|_{\text{outer}}/|k^2|_{\text{inner}} = 0.5 \to 2$), spurious solutions are less likely to be computed with (2) and their occurrence is essentially independent of the phase angles of the $k^2$'s. However, the smaller/larger the magnitudes of $k^2\Delta x^2$, the tighter/looser the restrictions become on size ratio in order to maintain insensitivity to phase. For example, if $|k^2|\Delta x^2 \approx 0.005$, a size ratio of unity is needed. When the size ratio is broadened (e.g. $|k^2|_{\text{outer}}/|k^2|_{\text{inner}} = 5$), a reduction in spurious effects is observed as the phase angle is increased (removal or near removal requiring $\sigma/\omega\epsilon > 1$) provided the magnitude requirements are met. In the limit of size ratio approaching unity and a vanishingly small phase angle, the geometry collapses to a homogeneous region which excites a single mode that is apparently orthogonal to the parasitic modes. While it is important to recognize that these observations are strictly problem-dependent, they have obvious practical relevance and qualitatively agree with the idealized dispersion analyses of real-valued wavenumbers presented in [23].

Fortunately, desirable behavior results from the use of the extended weak form (5) regardless of whether parasitic solutions arise in (2) or not; hence, one need not fully characterize the occurrence of corruptions in (2) with respect to parameter space, $k^2\Delta x^2$. Since parasites can be found to occur in (2) for some boundary-value problems, its general use is suspect and the extended form (5) is always preferable. As shown in Fig. 4, the use of the extended weak form effectively eliminates both types of corruptions observed in Fig. 3, and the direct vector $\boldsymbol{E}$ solution now agrees with the parasite-free calculations of Fig. 2. This removal of parasitic solutions consistently occurred by invoking (5) for all of the combinations of parameters that we have investigated to date.

It is interesting to note that in Fig. 4(b) the homogeneous natural boundary condition $\nabla\cdot\epsilon^*\boldsymbol{E} = 0$ is applied, whereas in Fig. 4(a) this is insufficient to produce the desired solution and a stronger condition, $\boldsymbol{E}\cdot\hat{\boldsymbol{n}} = 0$, must be enforced at the outer boundary in order to reproduce the interior field shown in Fig. 2(a). Fig. 5 shows the solution which results when $\nabla\cdot\epsilon^*\boldsymbol{E} = 0$ is applied in the case of Fig. 4(a). The need for explicit enforcement of a condition on $\boldsymbol{E}\cdot\hat{\boldsymbol{n}}$ is not limited to the geometry of Fig. 1(a), but occurs in the problem of Fig. 1(b) under certain circumstances as well. Fig. 6 shows such a case, for which the desired benchmark solution appears in Fig. 7. This solution can be retrieved via (5) if, as in

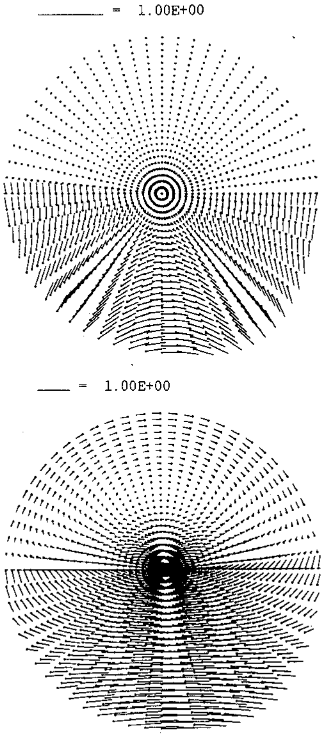

Fig. 5. Same as Fig. 4(a) except that the homogeneous natural boundary condition $\nabla \cdot \epsilon^* \boldsymbol{E} = 0$ is applied at the outer boundary. This solution is inconsistent with that of Figs. 4(a) and 2(a). Note the prominent appearance of a nonzero value of $\boldsymbol{E} \cdot \hat{\boldsymbol{n}}$ at the outer boundary.

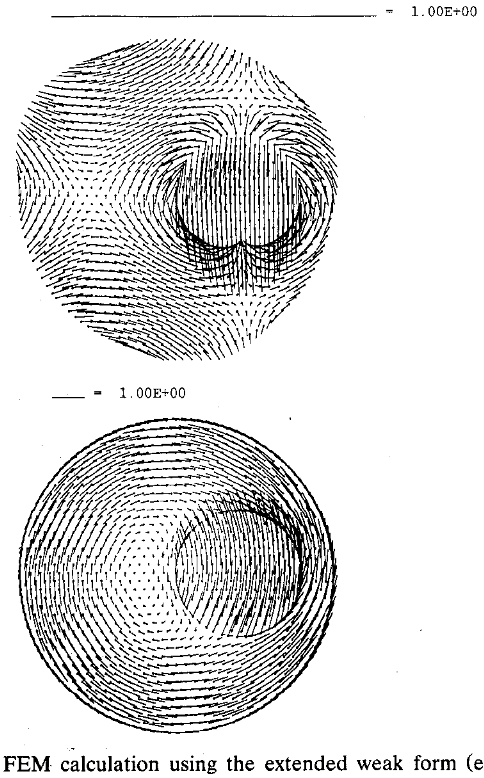

Fig. 6. FEM calculation using the extended weak form (eq. (5)) and the homogeneous natural boundary condition $\nabla \cdot \epsilon^* \boldsymbol{E} = 0$ on the off-center cylinder geometry of Fig. 1(b). The resultant solution is inconsistent with the benchmark solution (compare with Fig. 7). The complex wavenumbers in this case are $k^2_{\text{Inner}} = (0.02, 0.0)$ and $k^2_{\text{Outer}} = (0.090, 0.178)$. As in Fig. 5, a nonzero value of $\boldsymbol{E} \cdot \hat{\boldsymbol{n}}$ is computed at the outer boundary.

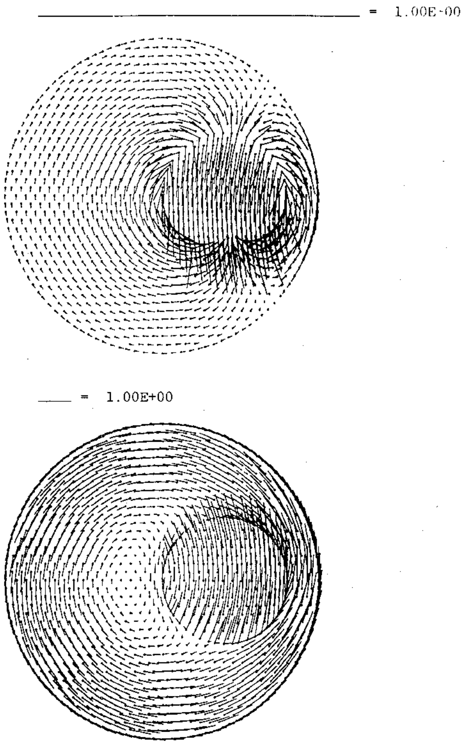

Fig. 7. Benchmark solution for the boundary-value problem of Fig. 6.

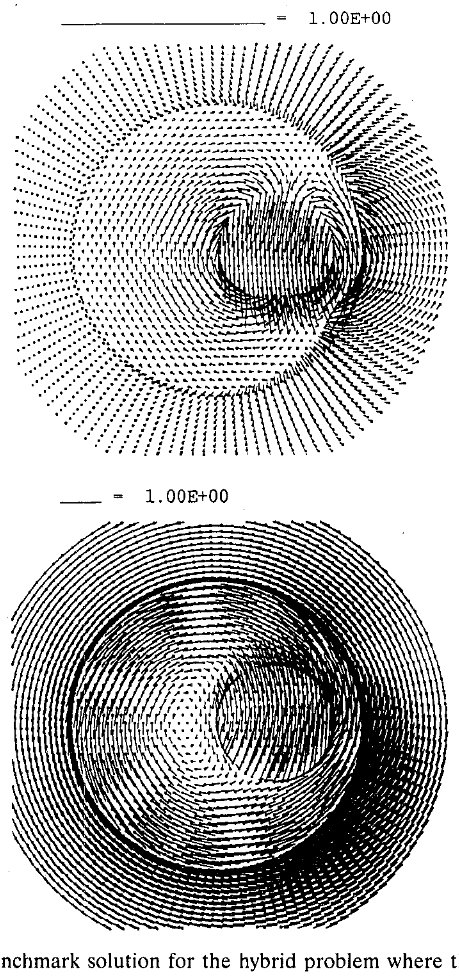

Fig. 8. Benchmark solution for the hybrid problem where the exterior solution is coupled to the interior solution through a uniform physical current imposed at the outer boundary. The $k^2$'s on the interior are identical to those of Fig. 6 while $k^2_{\text{exterior}} = (0.02, 0.0)$. Note the nonzero $\boldsymbol{E} \cdot \hat{\boldsymbol{n}}$ which occurs at the outer boundary.

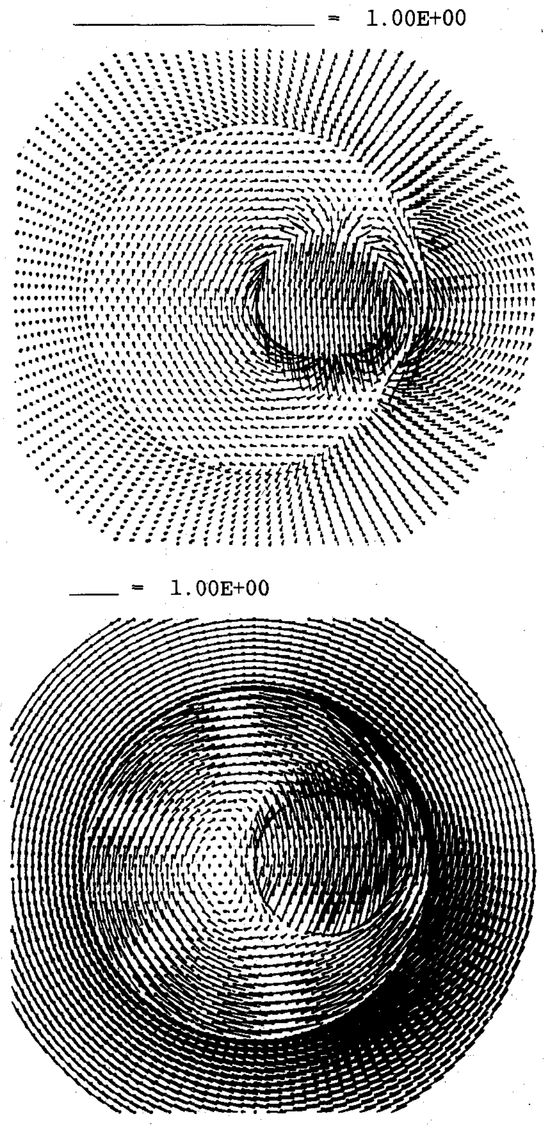

Fig. 9. Same as Fig. 8 except that a hybrid calculation using the extended weak form (eq. (5)) on the interior and the homogeneous natural boundary condition $\nabla\cdot\epsilon^*\boldsymbol{E} = 0$ on the outer boundary is used. This solution is consistent with the benchmark solution of Fig. 8.

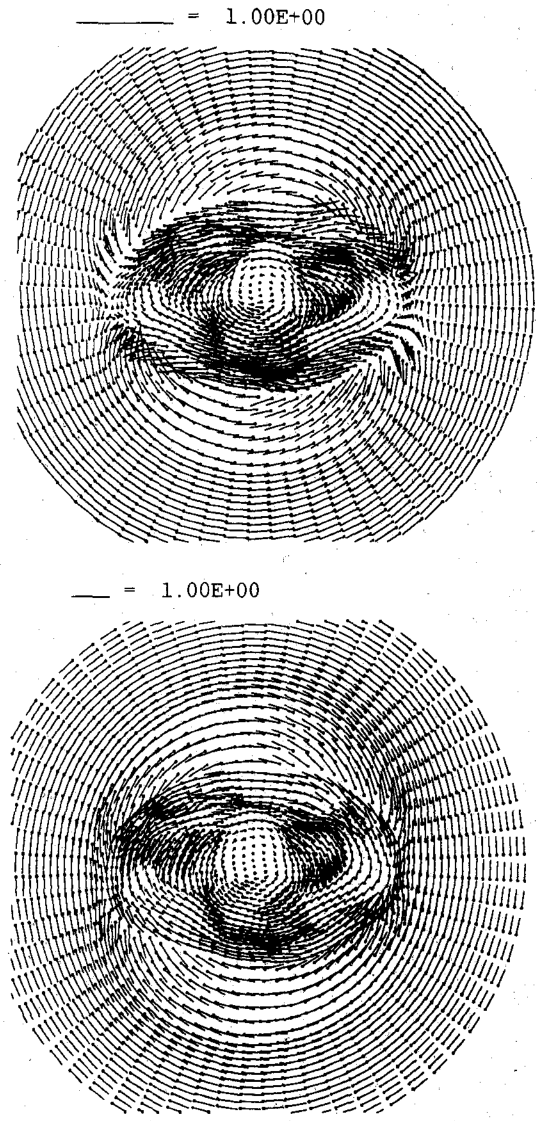

Fig. 10. Benchmark solution for a hybrid problem where a patient cross section is enclosed by a uniform current imposed at $R = 25$ cm. The body is electrically and geometrically complex (see [25]). Vector plots of $\mathrm{Re}(\boldsymbol{E})$ (top) and $\mathrm{Im}(\boldsymbol{E})$ (bottom) are shown. Vector length is proportional to strength (max scaled to unity).

Fig. 4(a), $\boldsymbol{E}\cdot\hat{\boldsymbol{n}} = 0$ is applied at the outer boundary. The distinctive feature of the $\nabla\cdot\epsilon^*\boldsymbol{E} = 0$ solution, when it fails to reproduce the benchmark, is the appearance of a nonzero $\boldsymbol{E}\cdot\hat{\boldsymbol{n}}$ at the outer boundary. The required enforcement of $\boldsymbol{E}\cdot\hat{\boldsymbol{n}} = 0$ implies that $\nabla\cdot\epsilon^*\boldsymbol{E} \neq 0$ in these cases; i.e., an equivalent charge is necessary to obtain a solution consistent with the benchmark solution.

It is important to avoid the characterization of the spurious solutions in Figs. 5 and 6 as vector parasites. In fact, they reveal subtle and unphysical features of the benchmark *boundary conditions*. Since the benchmark $\boldsymbol{E}$ is obtained from the curl of $\boldsymbol{H}$, its normal component is guaranteed to vanish along the prescribed constant-$\boldsymbol{H}$ boundary, irrespective of the computed interior solution; in effect, $\boldsymbol{E}\cdot\hat{\boldsymbol{n}} = 0$ is enforced as a Dirichlet boundary condition. In the Appendix we demonstrate that for an inhomogeneous cylinder, this set of boundary conditions implies variable current and nonzero charge at the boundary, which can only be deduced in detail after the interior solution is obtained. As an induction heating problem, this benchmark itself is, strictly speaking, unphysical, a solution in search of a source. It is better viewed simply as a useful boundary value problem with $H_z = 1$ and $\boldsymbol{E}\cdot\hat{\boldsymbol{n}} = 0$. In reproducing this benchmark with a vector calculation, $\boldsymbol{E}\cdot\hat{\boldsymbol{n}} = 0$ is the correct boundary condition. $\nabla\cdot\epsilon^*\boldsymbol{E} = 0$ might serendipitously produce $\boldsymbol{E}\cdot\hat{\boldsymbol{n}}$ nearly $= 0$, but in general it is wrong and potentially misleading because it corresponds to distinctly different and spurious forcing.

A measure of physical reality is restored to the benchmark computations through the use of a boundary integral expression for the external field, as in [24]. This removes the conceptual problems associated with specification of $\nabla\cdot\epsilon^*\boldsymbol{E}$ or $\boldsymbol{E}\cdot\hat{\boldsymbol{n}}$ as normal boundary conditions, and instead makes explicit the assumptions about the *physical* source currents and charges. In the present case, the prescribed uniform

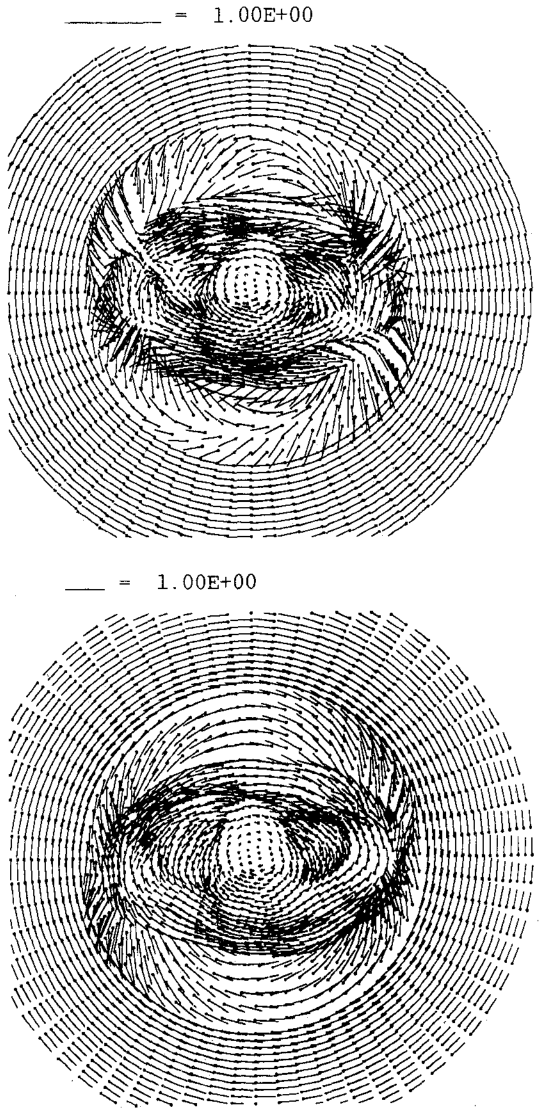

Fig. 11. Same as Fig. 10 except that the conventional double-curl formulation (2) governs the interior solution. Some significant departures from the benchmark solution can be seen.

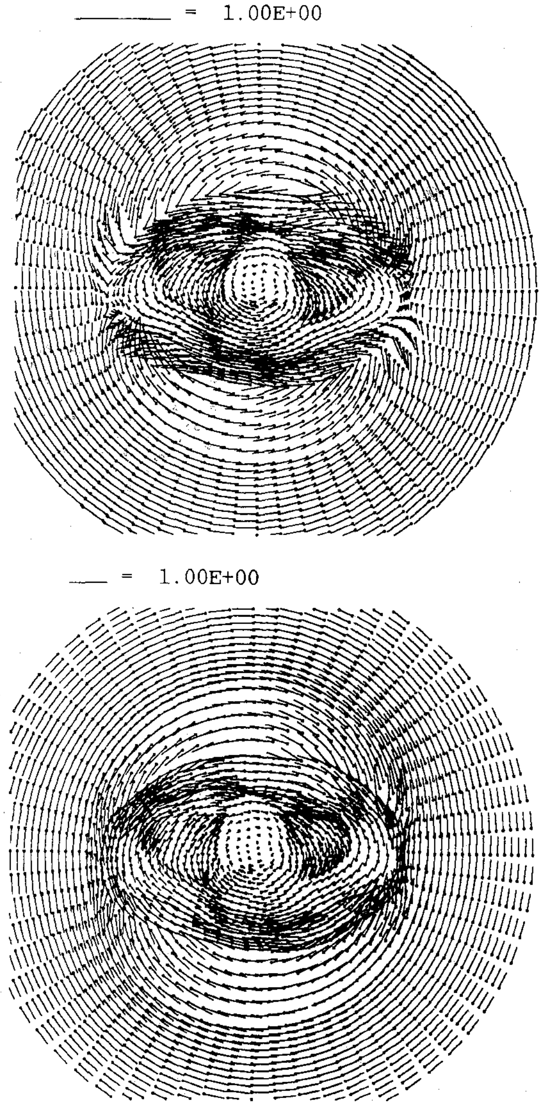

Fig. 12. Same as Fig. 10 except that the extended weak form (5) governs the interior solution. The calculation is in excellent agreement with the benchmark solution in Fig. 10.

equivalent current ($H_z$) used to drive the interior problem is replaced by uniform physical coupling conditions $J = 1$, $\rho = 0$, and $H_z$ is now allowed to vary circumferentially around both sides of the boundary. Figs. 8 and 9 show that the benchmark and the extended weak form solutions are in excellent agreement for the same dielectric cylinders as in Fig. 6. This coupled problem is physically different than the boundary-value problems in Figs. 6 and 7. The interior solution is in balance with both the exterior solution and the imposed physical sources through the electromagnetic jump conditions; the construction of artificial equivalent sources (boundary conditions) which lump both effects together *a priori* is unnecessary. The physical realism is limited only by the assumed uniformity of $\rho$ and $J$ on the boundary, representing a standard idealized device. For a more realistic device model one could introduce impedance and continuity relations among $\rho$, $J$, and $E$ on the boundary.

As a final example, we show a realistic calculation in a patient cross section in hybrid form. The computational domain is geometrically complex and contains six electrically distinct regions. Details of the geometry and the electrical properties can be found in [25]. The benchmark solution (Fig. 10) is supplied as well as the corrupted (Fig. 11) and corruption-free (Fig. 12) solutions. The extended weak form can be seen to behave admirably in this geometrically and electrically difficult problem.

## IV. CONCLUSIONS

Spurious vector modes occur with destructive strength in FEM boundary-value problems. The proposed strategy for their elimination is an expanded weak form which combines the double-curl and grad–div equations, with no required constraints on the finite element basis. The expanded weak form reduces the algebraic double-curl operator to a Galerkin Laplacian on homogeneous subregions, with modifications at boundaries to accommodate natural boundary conditions. Original tangential boundary conditions associated with the double-curl operator are retained while the grad–div operator introduces new boundary conditions on the normal field. The posing of the additional normal boundary condition actually demands no extra information. For example, when Neumann tangential boundary conditions are given, (i.e., $\nabla \times \boldsymbol{E}$, or equivalently tangential $\boldsymbol{H}$), the normal component of $\boldsymbol{E}$ is known exactly, *a priori*; hence, a Dirichlet condition on $E_n$ is available. Similar arguments can be made when Dirichlet conditions on tangential $\boldsymbol{E}$ are given [23]. The new weak form has been implemented on simple $C^0$ scalar bases, which preserves conservation of energy, explicit enforcement of boundary conditions on both normal and tangential field components, and coupling to exterior solutions. The new approach requires only simple extensions to the conventional double-curl formulation which can be implemented with minor programming changes in the element assembly.

Computational experiments reveal two types of spurious modes in driven problems, both of which have been noted previously in the normal mode context and are predicted in our dispersion analyses in [23]. The first, type A, is well resolved and has obvious divergence; the second, type B, appears at or near the mesh cutoff point $\lambda = 2\Delta x$ and is poorly resolved. Their occurrence is directly related to the size of $k^2\Delta x^2$, with larger values more immune than smaller ones. In multimedia problems, the size ratio of the $k^2$'s is also important (with values near unity the most spurious-mode-resistant) whereas their respective phase angles are less influential. The expanded weak form advocated here successfully removes both types of modes regardless of the $k^2\Delta x^2$ sizes, size ratios, or phase angles.

In some cases the homogeneous natural condition $\nabla \cdot \epsilon^* \boldsymbol{E} = 0$ is inappropriate as a boundary condition, indicating the need for an equivalent boundary charge to properly represent the assumed (perhaps unphysical) external field. In these cases the coupling of the FEM to the external environment in hybrid fashion allows the use of physically meaningful charges and currents, and makes the physical assumptions about the source explicit and unambiguous. These hybrid solutions exhibit nonzero normal $\boldsymbol{E}$ and extreme care is required in posing them unambiguously as pure boundary-value problems, irrespective of the chosen method of solution. In the examples reported here, both scalar and vector hybrid computations agreed; however the two boundary value problem solutions did not agree with each other or with the physically correct hybrid solution, owing to the nonequivalence of the various sets of boundary conditions.

Experimental attention has been restricted to 2-D; however our formulation (5) is fully 3-D and we anticipate that the general conclusions reached here will carry over to 3-D. We have recently implemented the time-domain equivalent of (5) in 3-D [25] and have demonstrated 3-D hybrid coupling with the method of moments [18]. In both instances we have found the results to be free of spurious fields. Furthermore, controlled studies aimed at identifying spurious 3-D vector modes are presently under way.

## APPENDIX

Here we demonstrate that variable current $J$ and nonzero charge $\rho$ are required to sustain the boundary conditions $H_z = 1$, $E_n = 0$ on an inhomogeneous cylinder in an infinite homogeneous medium. TE conditions are assumed; $(n,t)$ are the local normal and tangential coordinates in the plane. On the interior of the cylinder boundary we have, by hypothesis,

$$H_z = 1 \tag{A1}$$

$$E_n = 0 \tag{A2}$$

and since the cylinder is inhomogeneous, $E_t$ will generally be variable:

$$E_t = f(t). \tag{A3}$$

Applying the electromagnetic jump conditions, we obtain the fields on the outside of the boundary source:

$$H_z = 1 - J \tag{A4}$$

$$\epsilon^* E_n = \rho \tag{A5}$$

$$E_t = f(t). \tag{A6}$$

The Maxwell equation $-i\omega\epsilon^* \boldsymbol{E} = \nabla \times \boldsymbol{H}$ on the outside of the boundary gives

$$i\omega\epsilon^* E_t = \frac{\partial H_z}{\partial n} = i\omega\epsilon^* f(t) \tag{A7}$$

$$i\omega\epsilon^* E_n = -\frac{\partial H_z}{\partial t} = i\omega\rho. \tag{A8}$$

Equation (A7) is sufficient to completely specify $\boldsymbol{H}$ on the exterior; since this is a uniform medium with a cylindrical boundary, we infer that $H_z = H_z(t)$ and that constant $H_z$ on the exterior is incompatible with (A7) unless $f(t)$ is constant. From (A4) we conclude in turn that $J = J(t)$, and from (A8) that $\rho \neq 0$ and $E_n \neq 0$ on the exterior of the boundary.

The argument fails when $f(t)$ is constant, i.e., when $E_t$ does not vary on the interior of the cylinder boundary. In this case the conditions $H_z = 1$, $E_n = 0$ are compatible with constant $J$ and $\rho = 0$. For nearly homogeneous cylinders this suggests that $\rho = 0$ is a close approximation to $E_n = 0$, which explains the adequacy of $\rho = 0$ observed in some of the test cases.

## REFERENCES

[1] Z. J. Cendes and P. P. Silvester, "Numerical solution of dielectric loaded waveguides: I—Finite element analysis," *IEEE Trans. Microwave Theory Tech.*, vol. MTT-18, pp. 1124–1131, 1970.

[2] D. G. Corr and J. B. Davies, "Computer analysis of the fundamental and higher order modes in single and coupled microstrip," *IEEE Trans. Microwave Theory Tech.*, vol. MTT-20, pp. 669–678, 1972.

[3] A. Konrad, "A method for rendering 3D finite element vector field solutions non-divergent," *IEEE Trans. Magn.* vol. 25, pp. 2822–2824, 1989.

[4] J. A. M. Svedin, "A numerically efficient finite element formulation for the general waveguide problem without spurious

modes," *IEEE Trans. Microwave Theory Tech.*, vol. 37, pp. 1708–1715, 1989.

[5] J. B. Davies, F. A. Fernandez, and G. Y. Philippou, "Finite element analysis of all modes in cavities with circular symmetry," *IEEE Trans. Microwave Theory Tech.*, vol. MTT-30, pp. 1975–1980, 1982.

[6] R. L. Ferrari and G. L. Maile, "Three-dimensional finite element method for solving electromagnetic field problems," *Electron. Lett.* vol. 14, pp. 467–468, 1978.

[7] A. Konrad, "A direct three-dimensional finite element method for the solution of electromagnetic fields in cavities," *IEEE Trans. Magn.*, vol. MAG-21, pp. 2276–2279, 1985.

[8] C. W. Crowley, P. P. Silvester, and H. Hurwitz, "Covariant projection elements for 3D vector field problems," *IEEE Trans. Magn.*, vol. 24, pp. 397–400, 1988.

[9] A. R. Pinchuk, C. W. Crowley, and P. P. Silvester, "Spurious solutions to vector diffusion and wave field problems," *IEEE Trans. Magn.*, vol. 24, pp. 158–161, 1988.

[10] S. H. Wong and Z. J. Cendes, "Combined finite element-modal solution of three-dimensional eddy current problems," *IEEE Trans. Magn.*, vol. 24, pp. 2685–2687, 1988.

[11] S. H. Wong and Z. J. Cendes, "Numerically stable finite element methods for Galerkin solution of eddy current problems," *IEEE Trans. Magn.*, vol. 25, pp. 3019–3021, 1989.

[12] D. R. Lynch, K. D. Paulsen, and J. W. Strohbehn, "Finite element solution of Maxwell's equations for hyperthermia treatment planning," *J. Computat. Phys.*, vol. 58, pp. 246–269, 1985.

[13] K. D. Paulsen, D. R. Lynch, and J. W. Strohbehn, "Three-dimensional finite, boundary, and hybrid element solutions of the Maxwell equations for lossy dielectric media," *IEEE Trans. Microwave Theory Tech.*, vol. 36, pp. 682–693, 1988.

[14] C. W. Crowley and P. P. Silvester, "Comments on three-dimensional finite, boundary, and hybrid element solutions of the Maxwell equations for lossy dielectric media," *IEEE Trans. Microwave Theory Tech.*, vol. 36, p. 145, 1988.

[15] M. L. Barton and Z. J. Cendes, "New vector finite elements for three-dimensional magnetic field computation," *J. Appl. Phys.*, vol. 61, pp. 3919–3921, 1987.

[16] A. F. Peterson, "Finite element solution of the vector wave equation using divergencelss basis function," in *Proc. 1989 IEEE AP-S Int. Symp.*, vol. III, pp. 1624–1627.

[17] A. Bossavit, "Solving Maxwell equations in a closed cavity and the question of spurious modes," *IEEE Trans. Magn.*, vol. 25, pp. 702–705, 1990.

[18] X. Yuan, D. R. Lynch, and K. D. Paulsen, "Importance of normal field continuity in inhomogeneous scattering calculations," *IEEE Trans. Microwave Theory Tech.*, to be published.

[19] B. M. A. Rahman and J. B. Davies, "Penalty function improvement of waveguide solution by finite elements," *IEEE Trans. Microwave Theory Tech.*, vol. MTT-32, pp. 922–928, 1984.

[20] M. Koshiba, K. Hayata, and M. Suzuki, "Finite element formulation in terms of the electric field vector for electromagnetic waveguide problems," *IEEE Trans. Microwave Theory Tech.*, vol. MTT-30, pp. 900–905, 1985.

[21] J. P. Webb, "The finite element method for finding modes of dielectric loaded cavities," *IEEE Trans. Microwave Theory Tech.*, vol. MTT-33, pp. 635–639, 1985.

[22] A. Konrad, "On the reduction of the number of spurious modes in the vectorial finite-element solution of three-dimensional cavities and waveguides," *IEEE Trans. Microwave Theory Tech.*, vol. MTT-34, pp. 224–227, 1986.

[23] D. R. Lynch and K. D. Paulsen, "Origin of vector parasites in numerical Maxwell solutions," pp. 383–394, this issue.

[24] D. R. Lynch, K. D. Paulsen, and J. W. Strohbehn, "Hybrid element method for unbounded problems in hyperthermia," *Int. J. Numer. Meth. Eng.* vol. 23, pp. 1915–1937, 1986.

[25] D. R. Lynch and K. D. Paulsen, "Time-domain integration of the Maxwell equations on finite elements," *IEEE Trans. Antennas Propagat.*, vol. 38, pp. 1933–1942, Dec. 1990.

**Keith D. Paulsen** (S'85–M'86) received the B.S. degree in biomedical engineering from Duke University, Durham, NC, in 1981, and the M.S. and Ph.D. degrees in engineering from Dartmouth College, Hanover, NH, in 1984 and 1986, respectively.

He is currently an Assistant Professor in the Thayer School of Engineering at Dartmouth College. His research interests include numerical electromagnetics with application to biomedical problems.

**Daniel R. Lynch** received the B.S. and M.S. degrees in mechanical engineering from the Massachusetts Institute of Technology, Cambridge, in 1972 and the M.S. and Ph.D. degrees in civil engineering from Princeton University, Princeton, NJ, in 1976 and 1978, respectively.

He has worked as a power engineer and biomedical engineer, and he is currently Professor at Dartmouth College's Thayer School of Engineering, where he has taught since 1978. His interests are in environmental engineering and numerical analysis.